From tomography to mechanics: quantifying corrosion-induced splitting stresses in reinforced mortar

Materials and Structures (2026) 59:184
https://doi.org/10.1617/s11527-026-03082-9

ORIGINAL ARTICLE

From tomography to mechanics: quantifying corrosion-induced splitting stresses in reinforced mortar

Andreas Alhede · Jelke Dijkstra · Karin Lundgren

Received: 20 November 2025 / Revised: 16 February 2026 / Accepted: 31 March 2026

Abstract Corrosion of steel reinforcement is a major cause of deterioration in concrete structures, yet the mechanical response at the steel-mortar interface remains insufficiently understood. This study introduces an image-informed mechanics framework that quantifies the stress–strain behaviour of the corrosion layer and its role in cover cracking. X-ray and neutron computed tomography of a reinforced mortar specimen were used to determine corrosion-induced displacements at the steel-mortar interface. These image-derived displacements were applied as boundary conditions in non-linear finite element analyses that closely reproduced the geometry and loading conditions of the tested specimen, enabling evaluation of the stress–strain response of the corrosion layer. Two cases were analysed: one in which all corroded regions contributed to stress build-up, and one where expansion in regions containing interfacial voids was reduced to account for (near) stress-free expansion into these voids. The analyses revealed that radial stresses at the steel-mortar interface are strongly non-uniform, with only a few corroded regions dominating stress build-up. The quantified stress–strain response of the corrosion layer exhibited a non-linear mechanical behaviour, characterised by an apparent non-linear stiffness that increased with increasing strain, consistent with earlier mechanical characterisations. Overall, this image-informed mechanics framework offers new insights into the stress–strain behaviour of the corrosion layer. The results clarify parameters that govern crack propagation and provide quantitative measures to support future modelling and durability assessment of reinforced concrete.

Keywords Reinforced mortar · Steel corrosion · Image-based modelling · Corrosion-induced cracking

1 Introduction

Corrosion of steel reinforcement is a leading cause of deterioration in reinforced concrete structures [1], contributing to cracking, reduced bond strength, and reduced ultimate capacity [2, 3]. While numerous studies have investigated performance indicators of corrosion damage, such as the possible relationship between surface crack width and steel loss [4–6], these correlations are difficult to generalise and do not capture the underlying physical processes – particularly the development of internal stresses at the steel-concrete interface that drive cracking.

In recent years, X-ray and Neutron Computed Tomography (XCT, NCT) have gained increasing attention for the study of cementitious materials [7, 8]. These non-destructive techniques allow internal

Jelke Dijkstra and Karin Lundgren have contributed equally to this work.

A. Alhede (✉) · J. Dijkstra · K. Lundgren
Department of Architecture and Civil Engineering, Chalmers University of Technology, Gothenburg, Sweden
e-mail: andreas.alhede@chalmers.se

Published online: 09 April 2026

processes, such as phase transformations (e.g. steel corrosion) and concrete cracking, to be examined without altering the specimen. Beyond providing high-resolution three-dimensional images, typically at the micrometre scale, tomography has enabled quantitative analysis of corrosion penetration [9], crack widths [10], the influence of interfacial voids on pitting corrosion [11, 12], and volumetric strain in the rust [13]. Such studies of detailed imaging have opened new possibilities for investigating the evolution of corrosion-induced damage at the material scale (defined here as the scale at which specimens are geometrically suited for tomographic imaging while maintaining an image resolution at the micrometre scale).

However, tomography alone cannot provide mechanical quantities such as stress. While displacement fields and volumetric strain in the rust have been measured [13, 14], the internal stress state at the steel-mortar interface remains unresolved. Since stress development governs crack initiation and propagation, the absence of such data is a major limitation in the understanding of corrosion-induced cracking.

The present study addresses this limitation through an image-informed mechanics framework in which tomographic characterisation provides boundary kinematics for finite element analysis, enabling the mechanical response at the steel-mortar interface to be quantified. Building on recent multimodal tomography work on reinforced mortar specimens, experimentally derived measures of corrosion penetration, morphology and volumetric strains [14] are here used to prescribe displacement-driven boundary conditions in a numerical model. This makes it possible to investigate the stresses that develop at the steel-mortar interface.

The aim of this study was to characterise the stress–strain behaviour in the corrosion layer and the associated radial stresses at the steel-mortar interface. This approach links image-derived kinematics to mechanical response, providing new insight into how corrosion morphology drives stress localisation and crack formation.

2 Methodology

The numerical model used for the analyses presented in this study was based on experimentally derived data and implemented in a finite element framework to investigate the mechanical response of mortar subjected to steel corrosion. The modelling approach included two distinct loading cases and a separate parametric study using a full factorial design.

2.1 Experimental data

In the experimental campaign, accelerated corrosion was induced using an impressed current density of 50 μA/cm^2 for a total duration of four days. The corrosion process was monitored by measuring the electrical resistance of the specimen throughout the test. A sudden drop in electrical resistance, interpreted as the onset of cracking, was observed after approximately two days of applied current. Tomographic datasets were acquired prior to corrosion exposure and after the full four-day corrosion period. Accordingly, the numerical model corresponds to the final corrosion state.

The finite element model was informed by three-dimensional tomographic datasets of a reinforced mortar specimen [14]. From these images, spatially varying fields of the corrosion penetration depth (x), the volumetric strain in the rust (ε_v), the thickness of interfacial voids (f), and crack patterns were obtained. All quantities were discretised along the steel-mortar interface, with respect to both circumferential and longitudinal position (Fig. 1), and served as direct input for prescribing displacement-driven boundary conditions in the numerical simulations.

The volumetric strain was evaluated in three dimensions as the relative volume change ($\Delta V/V$) of the compressed corrosion layer, following the procedure described in [13]. Negative volumetric strains indicate compression of the corrosion layer relative to its free expansion. The magnitude of strain is primarily governed by the volumetric expansion coefficient of corrosion products and the confinement at the steel-mortar interface. For the specimen investigated in the present study, the volumetric expansion coefficient was experimentally quantified as $\eta = 3.84$ in [14].

2.2 Finite element model

The finite element analyses were performed using DIANA FEA 10.9 [15]. An overview of the geometry of the specimen used in the experimental campaign

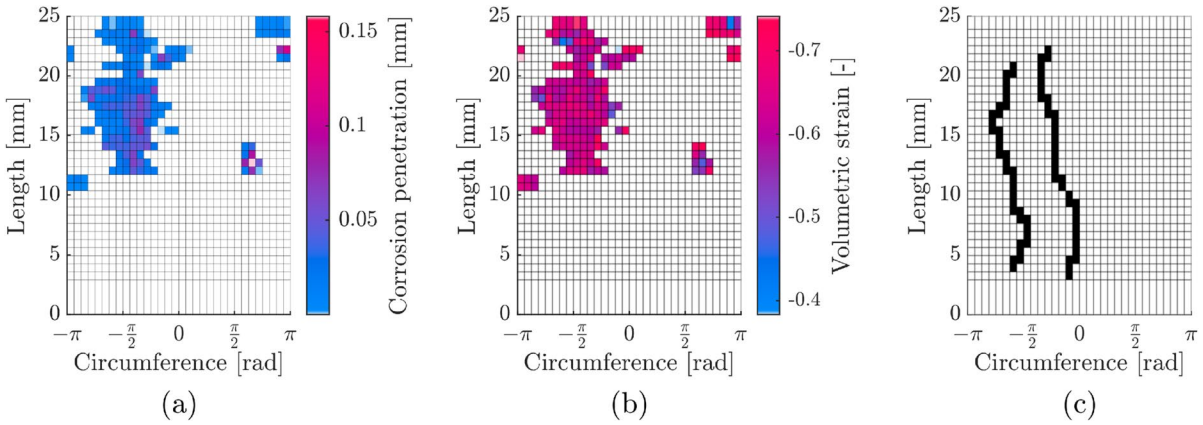

Fig. 1 Element-based representation of image-derived quantities at the steel-mortar interface. **a** Corrosion penetration depth, **b** volumetric strain in the rust and **c** crack pattern in the mortar adjacent to the steel-mortar interface. Data obtained from multimodal tomography of a reinforced mortar specimen [14]

and its numerical representation is shown in Fig. 2. The model applied discrete, spatially varying nodal displacements at the steel-mortar interface, based on the experimental measurements of corrosion penetration and volumetric strain in the rust.

To ensure stable crack localisation in the model, weakened material zones were introduced along selected regions of the steel-mortar interface. Without this measure, cracking tended to distribute over multiple adjacent elements, resulting in diffuse crack patterns and unrealistic energy dissipation. This is attributed to the use of isotropic and spatially uniform material properties in the model, which do not explicitly represent local heterogeneities and defects present in the experimental specimen. In reality, the mortar contains microcracks, interfacial voids and a material

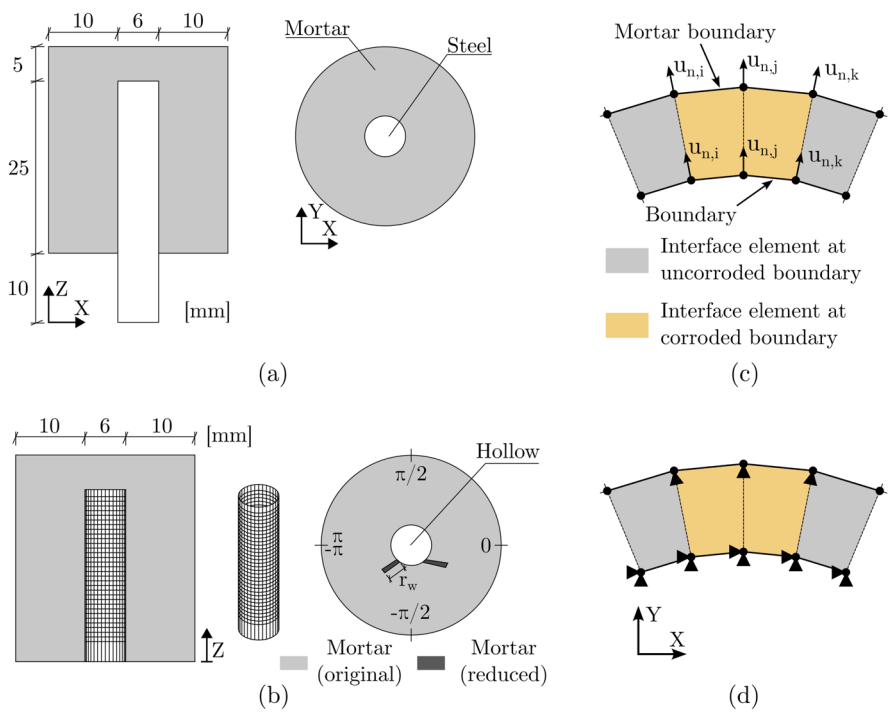

Fig. 2 Overview of the specimen geometry and its numerical implementation. **a** Geometry of the specimen in the experimental campaign, **b** geometry of the finite element model, **c** application of prescribed nodal displacements at the steel-mortar interface, **d** assignment of boundary conditions

variability that promote crack localisation. The weakened zones therefore represent these inherent heterogeneities in a simplified manner. They were placed in regions where cracking was observed experimentally (Fig. 1c), thereby allowing the model to reproduce the experimentally observed crack regions of the investigated specimen.

In these zones, the material parameters were reduced according to $f_w = \alpha f$, where f_w is the weakened material property, f is the bulk mortar property and α is the reduction factor. Both the reduction factor and the radial extent of this weakened zone (r_w, see Fig. 2b) were part of a full factorial design to examine their influence on cracking (outlined in Appendix A). The material properties of the bulk mortar are summarised in Table 1.

The reinforcement bar was not included in the model; instead it was assumed to be infinitely stiff compared to the mortar. Thus, only the outer surface area of the reinforcement bar was included; it was assumed to have zero deformations, and was discretised into a polygonal mesh consisting of 32 elements in the circumferential direction and 33 elements along the longitudinal axis of the bar, see Fig. 2. Each element was modelled using a 2D structural bending plate element, which is based on Kirchhoff's plate theory [17]. In other words, the surface area of the steel was modelled as a boundary in the analysis.

The mortar was modelled using 3D structural solid elements. The primary element type was 8-node isoparametric hexahedral element (HX24L), comprising 60.5 % of all solid elements. To accommodate the circular geometry of the specimens and mesh transitions, additional element types were used: 6-node prismatic elements (TP18L, 10.6 %), 5-node pyramid elements (PY15L, 16.1 %) and 4-node tetrahedral elements (TE12L, 12.8 %).

Table 1 Material properties used for the mortar in the finite element model

Property	Value / Basis
Compressive strength f_c [MPa]	35.6 [14]
Tensile strength f_{ct} [MPa]	3.3 [14]
Modulus of elasticity E_c [GPa]	31.5 [16]
Poisson's ratio ν	0.18 [16]
Fracture energy G_f [N/m]	69 [14]
Crack band width w_c [m]	Manually defined

Cracking was modelled using a smeared crack approach, incorporating a traction-separation law proposed by Hordijk [18, 19]. The crack bandwidth is commonly taken as the cube root of the element volume [15, 20], but this definition does not account for the element shape and can lead to errors when elements are elongated [21]. In the present model, crack localisation did not occur within a single band of elements, and a manually defined crack bandwidth was therefore adopted and applied consistently in all subsequent analyses. A rotating crack model was adopted, in which the crack normal aligned with the direction of the maximum principal strain [22]. The material behaviour in compression was modelled as perfectly elastoplastic, in order to prevent stress concentrations and localised crushing, which can occur due to mesh dependency in strain-softening constitutive models [23].

2.2.1 *Interface elements*

Plane interface elements were assigned between the boundary surface and the mortar. These interface elements are zero-thickness traction-separation elements that introduce two coincident nodes at each interface location: one associated with the mortar and one associated with the idealised boundary surface representing the mechanical constraint of the steel. Corrosion products were not explicitly modelled as a material phase. Instead, their expansive effect was represented kinematically by prescribing radial displacements, outlined in detail in Sect. 2.2.3.

The traction-separation formulation was defined in a local coordinate system, in which the normal direction was radial to the boundary surface, while the longitudinal and tangential directions were aligned with the vertical axis and circumference of the bar. The interface law was defined as

$$\begin{bmatrix} D_n & 0 & 0 \\ 0 & D_l & 0 \\ 0 & 0 & D_t \end{bmatrix} \begin{bmatrix} \Delta u_n \\ \Delta u_l \\ \Delta u_t \end{bmatrix} = \begin{bmatrix} t_n \\ t_l \\ t_t \end{bmatrix} \quad (1)$$

where Δu_n, Δu_l and Δu_t are the relative displacements in the normal, longitudinal and tangential directions of the interface, respectively, and t_n, t_l and t_t are the corresponding interface tractions. The stiffness matrix includes the normal stiffness, D_n, and shear stiffnesses in the longitudinal, D_l, and tangential, D_t, directions.

The interface was assumed to transmit compressive stresses effectively but to have less ability to carry tension. To represent this behaviour, a bilinear law was adopted for normal stresses, distinguishing between the compressive ($D_{n,c}$) and the tensile ($D_{n,t}$) response. This asymmetry reflects both the mechanical role of the interface and physical discontinuities such as microcracks, interfacial voids and local heterogeneities that reduce tensile resistance [24]. To select values of the stiffness parameters, a parameter study was carried out to assess the influence of interface stiffness on time-to-cracking and stresses at the steel-mortar interface. The investigated parameter bounds for $D_{n,t}$, $D_{n,c}$, D_l and D_t are given in Table 2. This study is further described in Appendix A.

2.2.2 *Boundary conditions*

Boundary conditions, illustrated in Fig. 2d, were applied to reflect the assumed mechanical behaviour of the model. Nodes associated with the boundary surface were fixed in all spatial directions. In contrast, mortar nodes in regions where corrosion took place were constrained only in the radial direction and remained free in the longitudinal and tangential directions. No constraints were applied to mortar nodes in regions without corrosion.

2.2.3 *Prescribed nodal displacements*

The expansion effect due to corrosion was simulated by applying spatially varying prescribed nodal displacements, $u_{n,i}$, at the steel–mortar interface in regions affected by corrosion.

The displacement formulation follows the radial strain formulation proposed by Lundgren [25], in which the radial strain in the corrosion layer is defined as

$$\varepsilon_{\text{cor}} = \frac{u_{n,\text{cor}} - a}{x + a} \tag{2}$$

where $u_{n,\text{cor}}$ is the radial displacement at the interface and x is the corrosion penetration depth. The term a denotes the free increase in radius under zero stress, defined as

$$a = -r + \sqrt{r^2 + (\eta - 1)(2rx - x^2)} \tag{3}$$

where r is the steel radius and η is the free volumetric expansion coefficient of the corrosion products.

Rearranging Eq. (2) gives

$$u_{n,\text{cor}} = \varepsilon_{\text{cor}}(x + a) + a. \tag{4}$$

In the present work, the experimentally determined volumetric strain in the rust, $\varepsilon_{v,i}$, was used as an approximation of the radial strain, i.e. $\varepsilon_{v,i} = \varepsilon_{\text{cor},i}$. All quantities were evaluated locally at each interface node i.

Given this assumption, the nodal displacement $u_{n,i}$ at each location i was calculated by

$$u_{n,i} = \varepsilon_{v,i}(x_i + a_i) + a_i - f_i \tag{5}$$

where x_i is the local corrosion penetration and f_i is the local average thickness of interfacial void.

The subtraction of f_i accounts for the unconfined expansion of corrosion products into interfacial voids, under the assumption that these voids allow free expansion without inducing pressure on the surrounding mortar. Note that for smaller voids, pressure may still develop once the void is filled, both in reality and in the model. In contrast, when f_i was sufficiently large to produce a negative $u_{n,i}$, the displacement was set to zero. This corresponds to the assumption that corrosion products can fully expand within the void space without exerting pressure on the surrounding mortar.

Two cases were considered:

- **Case 1, No void correction:** Interfacial voids were neglected, $f = 0$. The resulting nodal displacement field at the end of the analysis is shown in Fig. 3a.
- **Case 2, Void-corrected displacement:** Interfacial voids were explicitly accounted for using the thicknesses of the voids at the nodes evaluated from experiments shown in Fig. 3b. The adjusted displacement field at the end of the analysis is shown in Fig. 3c.

The time-dependent nature of corrosion propagation could not be resolved, as imaging data were available only at two discrete instances in time (before corrosion exposure and after the final corrosion state). Therefore, the spatial extent of the anodic region was

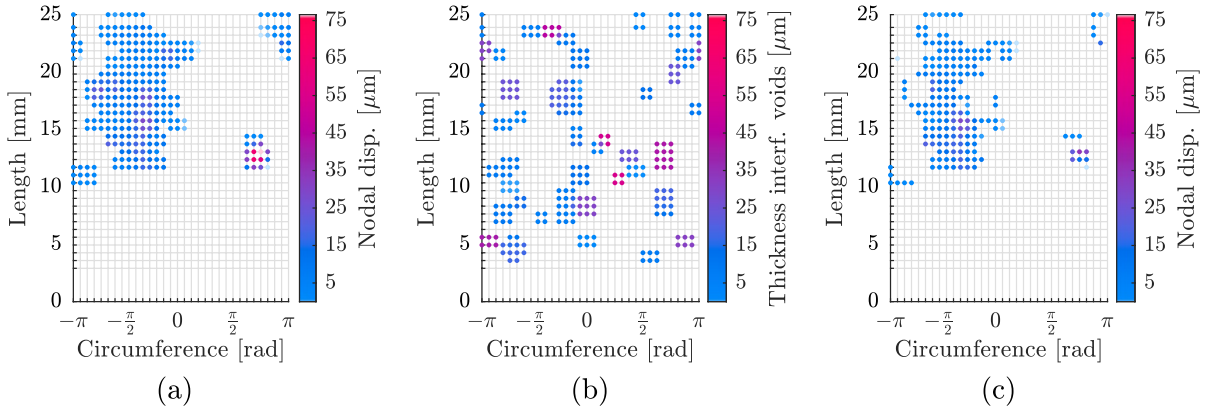

Fig. 3 Nodal representation of normal displacement and interfacial voids. **a** the normal displacement of the interface without accounting for interfacial voids **b** thickness of interfacial voids at each node **c** normal displacement of the interface, accounting for the presence of interfacial voids

assumed constant during the corrosion period, while corrosion penetration was assumed to increase progressively. The prescribed normal displacements were applied with a linear increase, representing a numerical loading path toward the experimentally observed final state. The model geometry corresponds to this final corrosion configuration obtained after the four-day accelerated corrosion period.

The normal displacement was applied radially outwards using a local coordinate system defined at each node. Owing to the use of interface elements between the mortar and the boundary surface, two coincident nodes were introduced at each interface location: one belonging to the the mortar and the other to the boundary. The prescribed displacement was applied equally to both nodes where corrosion took place, as illustrated in Fig. 2c.

In addition to the corrosion-induced displacements, autogenous shrinkage of the mortar was included in the model to represent the initial mechanical state of the specimen. It was implemented as a uniform volumetric contraction of the mortar applied prior to the onset of corrosion. The autogenous shrinkage strain $\varepsilon_{ca} = 0.056$ ‰, was estimated using an empirical expression provided in [26], which relates autogenous shrinkage to the strength class of the mortar.

The radial stress at the steel-mortar interface was calculated from the residual nodal forces at the interface. This was achieved by evaluating the internal force equilibrium between the two coincident nodes connected via the interface element, see Appendix B.

3 Results and discussion

A sensitivity study was carried out to examine the influence of the interface stiffness parameters $D_{n,t}$, $D_{n,c}$, D_l, and D_t as well as the reduction factor α and radial extent r_w of the weakened zones. The study is presented in Appendix A, and a representative parameter set (highlighted in Table 2) was selected for the subsequent analyses.

3.1 Mortar cracking

Figure 4a shows the surface crack patterns at the end of the corrosion period, observed in the experiment and obtained from the two modelling cases: with and without adjusting the prescribed nodal displacements to account for the presence of interfacial voids. The experimental results (triangles) reveal two longitudinal cracks located approximately 180° apart along the circumference of the bar. In addition, a transverse crack is visible between the two longitudinal cracks. The position of this transverse crack is not constant along the length of the specimen but follows a "V-shaped" trajectory.

When interfacial voids were not included in the model, the predicted crack pattern (diamonds) captured the main features observed in the experiment, including the two longitudinal cracks and the transverse crack. In the second modelling case, which accounted for the presence of interfacial voids (squares), the crack pattern also reflected the

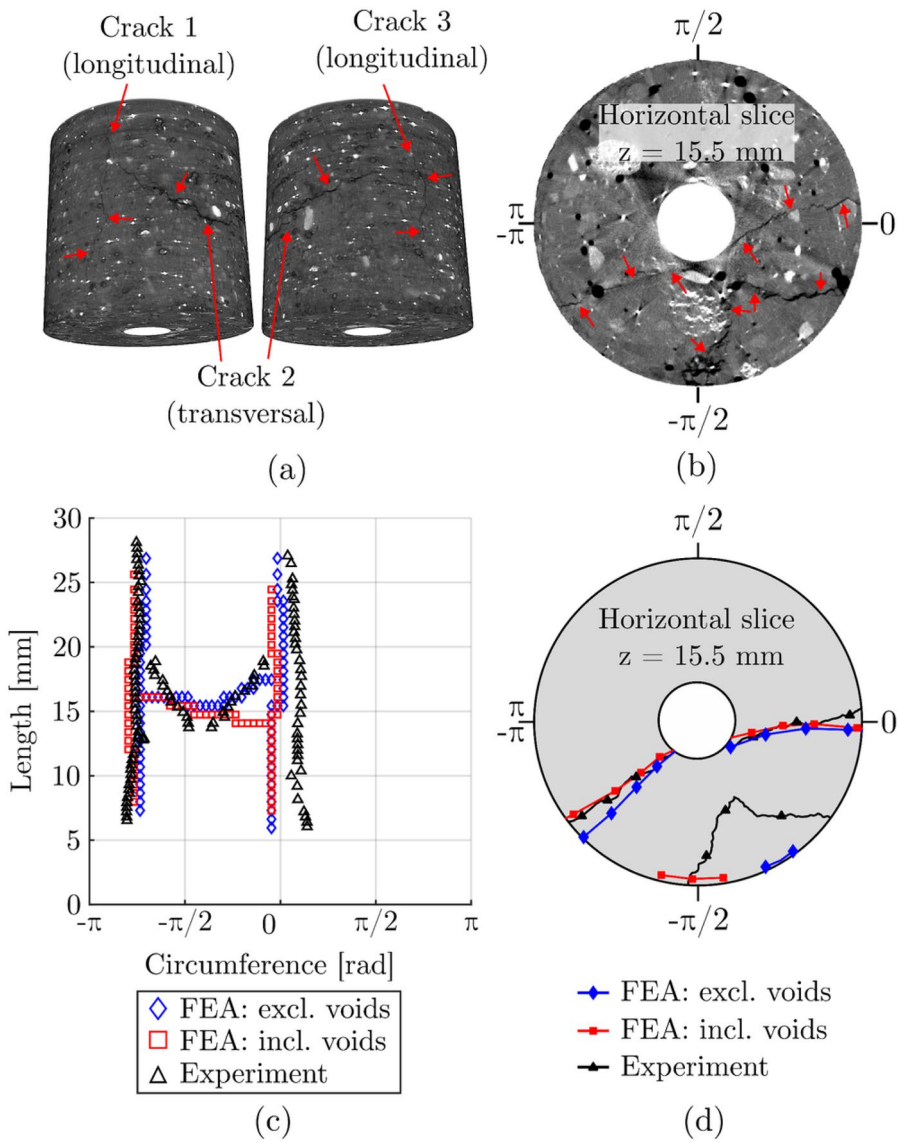

Fig. 4 Surface crack patterns and internal cracking of the investigated specimen. **a** Three-dimensional rendering of the XCT dataset illustrating two longitudinal cracks and one transverse crack. **b** Horizontal cross-sectional view at z = 15.5 mm showing experimental crack pattern in the cross-sectional plane. **c** Surface crack pattern as a function of circumference and specimen length. **d** Crack pattern at a cross-sectional slice at z = 15.5 mm

experimentally observed one. The transverse crack, however, followed a spiral path along the circumference rather than the V-shaped trajectory observed in the experiment.

The closer agreement between the experimental crack pattern and the model excluding interfacial voids indicates that, in reality, corrosion in regions containing interfacial voids contributes to stress development at the steel-mortar interface. Although interfacial voids provide initial space for free expansion, corrosion products have been observed to precipitate along the walls of such voids, forming a layer that grows inward and becomes mechanically constrained by the surrounding concrete. This can generate expansive pressure even if the void is not completely filled [27].

Figure 5 shows the displacement field within the mortar, as obtained from experimental measurements [14] and from finite element analyses for the two cases considered. In all cases, the displacement vectors indicate a localised expansion at mid-height, consistent with the location of the transverse crack observed in both the experiment and the finite element analyses. This bulging effect can be interpreted as an indication of crack development in that region, resulting from the localised corrosion pattern.

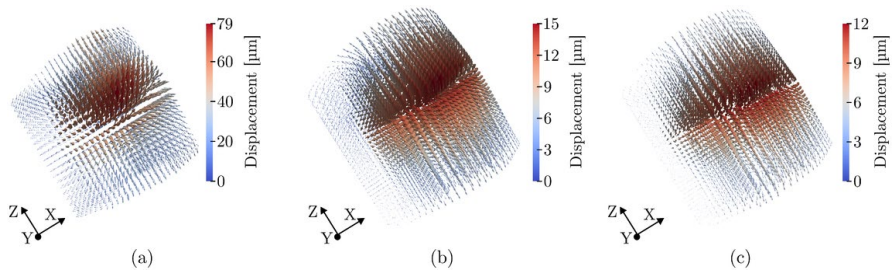

Fig. 5 Displacement field within the mortar cover. **a** Experimental results. **b** Finite element analysis without correction for interfacial voids. **c** Finite element analysis with correction for interfacial voids. Note that both the colour scales and vector magnitudes vary between subfigures and should not be directly compared

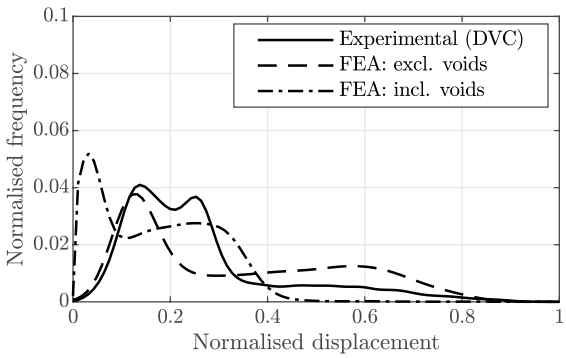

Fig. 6 Normalised kernel density estimates of nodal displacements in the mortar. Both the displacement values and the corresponding density estimates have been normalised by their respective maximum values to enable direct comparison between the cases

As can be seen in Fig. 5, the largest displacements were observed in the experimental results, with a maximum measured displacement of 79 µm. In contrast, the numerical analyses yielded lower displacements, with maxima of 15 µm and 12 µm for the cases with and without correction of the prescribed nodal displacements due to interfacial voids, respectively. Thus, there were differences in the extent and severity of cracking between the simulations and the experiment. In the experiment, the larger displacements may also reflect the influence of additional deformation mechanisms beyond the corrosion-induced deformations, such as local defects in the mortar not captured in the model.

Figure 6 shows the normalised kernel density estimates of nodal displacements for the experimental and numerical cases. The experimental distribution is relatively broad and exhibits two distinct peaks, followed by a tail of lower frequency and higher displacements. This tail is attributed to the local damage in the mortar, such as the transverse and longitudinal splitting cracks.

When interfacial voids were excluded in the model, the distribution showed a single dominant peak and a broader tail toward higher displacements, indicating a more localised deformation than in the experiment. However, the absolute displacement magnitudes were lower than those measured experimentally (compare Fig. 5). When the effect of interfacial voids were included in the model, the distribution of displacements differed from both the experimental and the modelling case where voids were excluded, showing a single distinct peak at low displacements, higher frequencies of intermediate displacements and no pronounced tail toward larger displacements.

3.2 Stress and strain in the rust

The distribution of radial stress was found to be largely insensitive to the stiffness parameters of the interface elements (Fig. 9). Across all analyses, the overall stress trends remained consistent, even after cracking had initiated in the surrounding mortar. The resulting radial stress distributions at the steel-mortar interface for the two cases are shown in Fig. 7. In both cases, high compressive radial stresses developed primarily in regions with significant corrosion. When the effect of interfacial voids were excluded (Fig. 7a), the maximum compressive stress exceeded 15 MPa. When the normal displacement was corrected to account for the presence of interfacial voids (Fig. 7b), the maximum compressive stress was lower, reaching about 11 MPa.

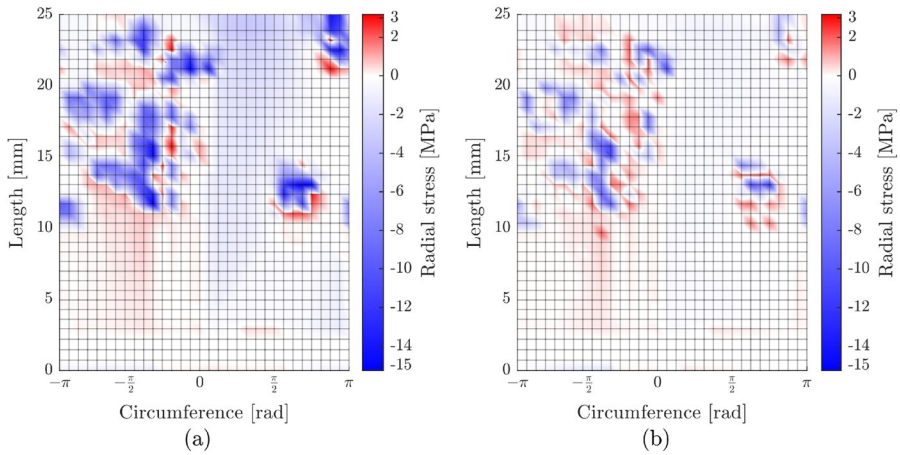

Fig. 7 Distribution of radial stress at the steel-mortar interface shown as a function of the circumferential and longitudinal positions along the steel. **a** Excluding and **b** including the effect of interfacial voids on the normal displacement

In both cases, smaller tensile stresses were observed adjacent to corroded regions. These stresses arose due to local compatibility of deformations, whereby prescribed normal displacements in corroded regions induced tension in neighbouring uncorroded areas through the continuous deformation of the surrounding mortar. Moreover, since corrosion was mostly concentrated on one side of the steel bar (from $-\pi$ to 0 radians), compressive radial stresses also developed on the opposite side. This occurred because the asymmetric expansion locally pushed the surrounding mortar toward the bar in regions without corrosion, resulting in smaller compressive stresses to maintain global equilibrium.

The relationship between stress and strain in the rust was further investigated by plotting the radial stress versus the corresponding volumetric strain, as determined experimentally. These results are shown in Fig. 8 for the two modelled cases. In both cases, the majority of data points correspond to volumetric strains in the range of −0.5 to −0.7 and radial stresses between +1.5 MPa and –2.5 MPa. As a reference, given that the volumetric expansion coefficient of the corrosion products was assumed $\eta = 3.84$, the volumetric strain would approach approximately $\varepsilon_v = -0.74$ if no displacement occurred at the interface. A subset of points displayed higher compressive stresses, with these values being approximately uniformly distributed over the range.

The results from both modelling cases indicate a non-linear behaviour of the corrosion products, i.e. the radial stress is not linearly depending on

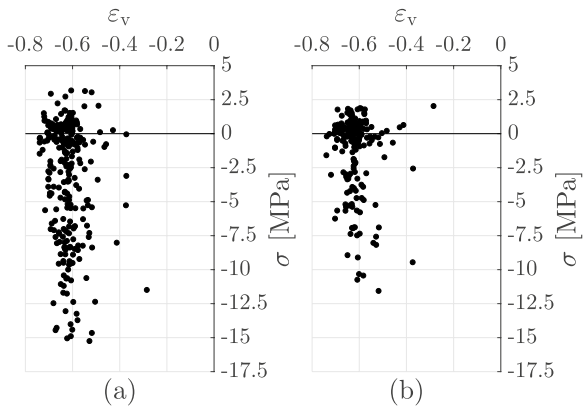

Fig. 8 Scatter plots illustrating the radial stress in corroded regions of the steel-mortar interface as a function of the volumetric strain. **a** Without correction for interfacial voids. **b** With correction for interfacial voids

the volumetric strain. Instead, the stiffness appears to increase with increasing strain magnitude. This agrees well with the observed behaviour in tests [28–30], and also with early estimations of Lundgren [25].

Further, it can be noted that there is some scatter in the data, including a number of points where tensile radial stresses were obtained despite negative (compressive) strain values. This may be attributed to the assumption introduced in Sect. 2.2.3, where the radial displacements in the analyses was calculated assuming that the volumetric strain equals the radial strain in the corrosion layer. In reality, the volumetric strain in the corrosion layer may also depend on local expansion or contraction of the corrosion products in

the directions along and transverse to the rebar. This probably took place along the edges of the corrosion pits; i.e. the rust formed in a pit could expand not only in radial direction but also in the directions along and transverse to the rebar. By including these effects in possible future modelling work, it may be possible to limit the number of data points in which tension is obtained, and possibly also to reduce the scatter.

Lastly, another contributing factor may be the continuity of the displacement field in the analyses. Nodes associated with uncorroded regions may have experienced tensile stresses due to compatibility requirements with adjacent nodes subjected to an imposed displacement (corroded regions). In such cases, one could argue that the normal stiffness of the interface in tension should have been assigned a lower value to limit the development of tensile stresses. Still, this work describes a novel and promising work flow enabling the evaluation of the mechanical response of corrosion products, and the results strongly indicate a non-linear behaviour.

4 Conclusions

This paper has demonstrated that an image-informed mechanics framework can translate tomographic observations into the mechanical response associated with steel corrosion in reinforced mortar. Whereas previous experimental investigations have mainly provided kinematic information, the present approach enables quantification of stresses and characterisation of the stress–strain response of the corrosion layer.

The following conclusions were drawn:

- Image-based data were used to quantify stresses at the steel-mortar interface, providing mechanical information beyond what imaging alone can deliver.
- In both cases analysed, compressive radial stresses were observed in corroded regions of the steel. Smaller tensile radial stresses appeared in regions adjacent to or between corroded areas, which are most likely a result of the modelling approach.
- The relationship between stress and strain in the rust was found to be non-linear; the stiffness appear to increase with increasing strain magnitude. Most data points were concentrated at lower stress levels, but some experienced higher compressive stresses, indicating that certain parts of the corroded regions may have contributed more significantly to the development of cracking.
- Both modelling cases reproduced the experimentally observed crack pattern, consisting of one transverse and two longitudinal cracks. The best agreement was obtained when the influence of voids on the prescribed nodal displacements was neglected, indicating that corrosion in regions containing interfacial voids still contributes to stress build-up at the steel-mortar interface.

Acknowledgements The computations enabled by resources provided by Chalmers e-Commons were greatly appreciated.

Funding Open access funding provided by Chalmers University of Technology. This project was financially supported by the Swedish Research Council Formas (grant no. 2022-01175) and the Swedish Transport Administration (grant no. 2024/62846).

Data availability The experimental data used in this study are made available at https://dx.doi.org.10.5291/ILL-DATA.1-07-1 after the embargo period (14-11-2028). The numerical data are available from the corresponding author upon request.

Declarations

Conflict of interest The authors declare that they have no conflict of interest.

Appendix A: Full factorial design

A Full Factorial Design (FFD) was performed to investigate the effect of the interface stiffness parameters $D_{n,t}$, $D_{n,c}$, D_l, and D_t as well as the reduction factor α applied to the weakened mortar zones and its radial extent r_w. Two response variables were evaluated: (1) the radial stress at the steel-mortar interface and (2) the displacement increment which caused onset of surface cracking (for which independent experimental data were available). In a full factorial design, all possible combinations of predefined parameter levels are evaluated [31].

Prior to the FFD, reference values were assumed for each stiffness parameter. Previous studies have proposed various values for the normal stiffness of the interface under compressive loading. For example, Lundgren [32] assumed a varying normal stiffness depending on the normal deformation, where the stiffness decreased with increasing deformation. Based on this approach, corresponding values in the range of 5×10^{11} N m^{-3} to 5×10^{12} N m^{-3} would be applicable in the present study. In contrast, Van Steen et al. [33] assumed a constant normal stiffness of 1×10^{12} N m^{-3}.

In the present study, the reference value of the normal stiffness for tensile stresses was chosen to $D_{n,t} = 3 \times 10^{11}$ N m^{-3}. This reference value was estimated by dividing the tensile strength of the mortar by the mean value of the prescribed nodal displacement. The reference value of the normal stiffness in compression was assumed to be $D_{n,c} = 3 \times 10^{12}$ N m^{-3}. The reference value of the longitudinal shear stiffness, D_l, was estimated from an assumed shear traction $t_l = 1.0$MPa and a corresponding relative displacement of the interface $\Delta u_{n,t} = 10\mu$m, resulting in $D_l = 1 \times 10^{11}$ N m^{-3}. To the best of the authors' knowledge, no experimental data are available for the tangential shear stiffness D_t, and it was therefore set equal to D_l. This assumption is further supported by the use of smooth steel bars in the experiment, where the absence of mechanical interlocking reduces anisotropy in the shear response along the interface.

In the FFD, each parameter was varied at two levels. It is important to note that these values were not intended to represent physical limits, but rather to define a reasonable range over which the influence of each parameter could be explored. Lower and upper bounds were defined for all six parameters – four stiffness parameters and two parameters describing the weakened zones – resulting in $2^6 = 64$ unique combinations. The values used in the FFD are summarised in Table 2, where the highlighted entries denote the values used in the final numerical model.

The results from the sensitivity study are presented in Fig. 9. Two response variables were evaluated: (1) the mean radial stress at the steel–mortar interface, and (2) the scaling factor of the total prescribed nodal displacements at which surface cracking occurred, defined as the point when the first principal strain exceeded 1×10^{-3} at the surface of the mortar. The scaling factor can be compared with the occurrence of surface cracking from electrical resistivity measurements, which was at approximately half of the time with applied corrosion current. Thus, a scaling factor at cover cracking of 0.52 indicates agreement with the experiment. Although not in perfect agreement with the experimental time-to-cracking, higher stiffness values combined with a larger r_w led to cracking at a lower scaling factor of the normal prescribed displacement. Further, the radial stresses were almost unaffected by the choice of the stiffnesses. Based on the observed trends, a combination of parameter values was selected for the subsequent analyses: $r_w = 3$mm, $\alpha = 0.8$, $D_{n,t} = 3 \times 10^{11}$ N m^{-3}, $D_{n,c} = 3 \times 10^{13}$ N m^{-3}, $D_l = \times 10^{12}$ N m^{-3} and $D_t = 1 \times 10^{11}$ N m^{-3}.

Appendix B: Radial stress at the steel-mortar interface

The radial stress at the steel-mortar interface was evaluated from the residual nodal forces. A free-body diagram of two coupled nodes is shown in Fig. 10 where $R_{boundary}$ and R_{mortar} represent the out-of-balance forces at the boundary and mortar nodes, respectively. The term F_{IF} denotes the internal force transmitted across the interface, while F_{mortar} corresponds to the internal force acting on the mortar node.

Table 2 Lower and upper bound values used in the parametric study for the radial extent of the weakened zone (r_w), the reduction factor (α) and the stiffness parameters in the interface elements: $D_{n,t}$, $D_{n,c}$, D_l and D_t. The **bold** entries denote the values used in the final numerical model

	r_w [mm]	α [–]	$D_{n,t}$ [N m^{-3}]	$D_{n,c}$ [N m^{-3}]	D_l [N m^{-3}]	D_t [N m^{-3}]
Low	2	0.4	3×10^{10}	3×10^{12}	1×10^{11}	$\mathbf{1 \times 10^{11}}$
High	**3**	**0.8**	$\mathbf{3 \times 10^{11}}$	$\mathbf{3 \times 10^{13}}$	$\mathbf{1 \times 10^{12}}$	1×10^{12}

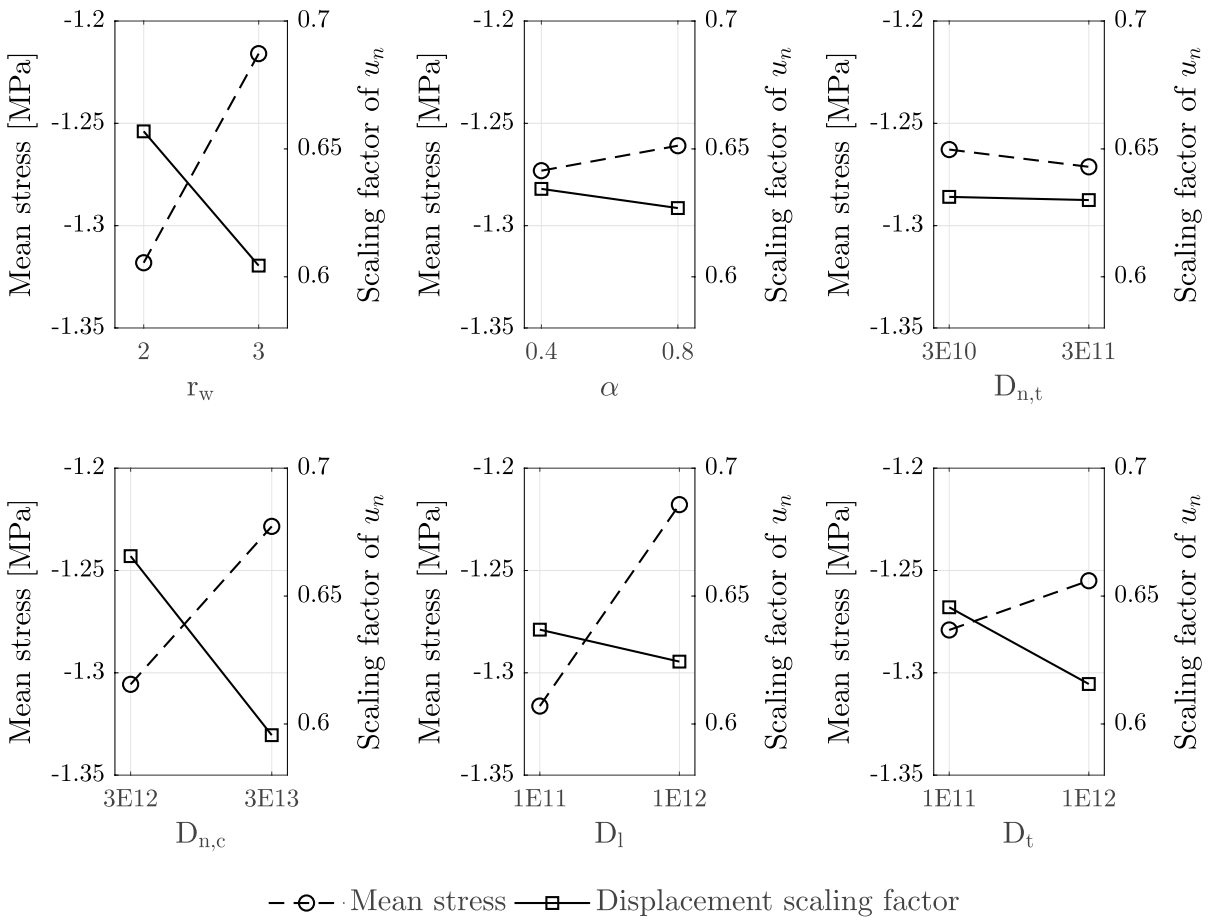

Fig. 9 Main effects plot from the full factorial design, showing the influence of r_w, α, $D_{n,t}$, $D_{n,c}$, D_l and D_t on the mean value of the radial stress at the mortar boundary (dashed line, left-hand axis) and the relative prescribed nodal displacement increment corresponding to the onset of surface cracking (solid line, right-hand axis)

By applying force equilibrium to the mortar node, the internal force F_{mortar} can be expressed as:

$$\begin{aligned} \uparrow \quad & R_{mortar} - F_{IF} - F_{mortar} = 0 \\ \Rightarrow \quad & F_{mortar} = R_{mortar} - F_{IF} \end{aligned} \tag{B1}$$

Substituting $F_{IF} = R_{boundary}$ from force equilibrium at the boundary node yields:

$$F_{mortar} = R_{mortar} - R_{boundary} \tag{B2}$$

The corresponding radial stress was calculated by dividing F_{mortar} by the associated nodal area. The contributing area was assumed to span to the centre point of each adjacent element in the transverse and longitudinal directions.

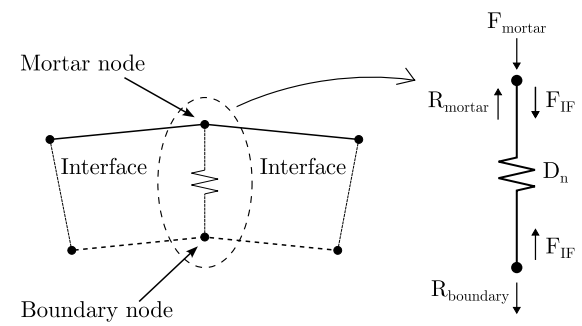

Fig. 10 A pair of nodes with corresponding forces acting on each node

References

1. Poursaee A, Hansson CM (2009) Potential pitfalls in assessing chloride-induced corrosion of steel in concrete. Cem Concr Res 39:391–400. https://doi.org/10.1016/j.cemconres.2009.01.015
2. Rodriguez J, Ortega LM, Garcia AM (1994) Assessment of structural elements with corroded rebars. Corros Corros Protect Steel Concrete 1:171–185
3. Lundgren K (2007) Effect of corrosion on the bond between steel and concrete: an overview. Mag Concr Res 59:447–461. https://doi.org/10.1680/macr.2007.59.6.447
4. Andrade C, Cesetti A, Mancini G, Tondolo F (2016) Estimating corrosion attack in reinforced concrete by means of crack opening. Struct Concr 17(4):533–540. https://doi.org/10.1002/suco.201500114
5. Tahershamsi M, Fernandez I, Lundgren K, Zandi K (2018) Investigating correlations between crack width, corrosion level and anchorage capacity. Struct Infrastruct Eng 13(10):1294–1307. https://doi.org/10.1080/15732479.2016.1263673
6. Kuntal VS, Jiradilok P, Nagai BJE, K, (2021) Estimating corrosion levels along confined steel bars in concrete using surface crack measurements and mesoscale simulations guided by model predictive control. Cement Concr Compos https://doi.org/10.1016/j.cemconcomp.2021.104233
7. Brisard S, Serdar M, Monteiro PJM (2020) Multiscale X-ray tomography of cementitious materials: a review. Cem Concr Res. https://doi.org/10.1016/j.cemconres.2019.105824
8. Zhang P, Wittmann FHP, Lura Müller HS, Han S, Zhao T (2018) Application of neutron imaging to investigate fundamental aspects of durability of cement-based materials: a review. Cem Concr Res 108:152–166. https://doi.org/10.1016/j.cemconres.2018.03.003
9. Van Steen C, Pahlavan L, Wevers M, Verstrynge E (2019) Localisation and characterisation of corrosion damage in reinforced concrete by means of acoustic emission and X-ray computed tomography. Constr Build Mater 197:21–29. https://doi.org/10.1016/j.conbuildmat.2018.11.159
10. Šavija B, Luković M, Hosseini SAS, Pacheco J, Schlangen E (2015) Corrosion induced cover cracking studied by X-ray computed tomography, nanoindentation, and energy dispersive X-ray spectrometry (EDS). Mater Struct 48:2043–2062. https://doi.org/10.1617/s11527-014-0292-9
11. Robuschi S, Tengattini A, Dijkstra J, Fernandez I (2021) A closer look at corrosion of steel reinforcement bars in concrete using 3D neutron and X-ray computed tomography. Cem Concr Res. https://doi.org/10.1016/j.cemconres.2021.106439
12. Wang Y, Miao X, Zhao Y, Peng L, Xu D, Mao J (2024) Quantitative image analysis on the filling proportion of corrosion products in reinforced concrete using X-ray computed tomography. Cement Concr Compos. https://doi.org/10.1016/j.cemconcomp.2024.105558
13. Alhede A, Dijkstra J, Robuschi S, Tengattini A, Lundgren K (2023) A two-stage study of steel corrosion and internal cracking revealed by multimodal tomography. Constr Build Mater. https://doi.org/10.1016/j.conbuildmat.2023.132187
14. Alhede A, Dijkstra J, Tengattini A, Lundgren K (2025) Characterisation of steel corrosion and matrix damage in reinforced mortar combining analytical, electrical and image-based techniques. Cem Concr Res. https://doi.org/10.1016/j.cemconres.2025.107792
15. DIANA FEA BV (2024) DIANA finite element analysis – theory manual, Release 10.9. Ferreira D, editor. Delft, The Netherlands: DIANA FEA BV
16. fib (2010) fib Model Code for Concrete Structures. International Federation for Structural Concrete
17. Timoshenko S, Woinowsky-Krieger S (1959) Theory of plates and shells, 2nd edn. McGraw-Hill, New York
18. Reinhardt H, Cornelissen H, Hordijk D (1986) Tensile tests and failure analysis of concrete. J Struct Eng 112(11):2462–2477. https://doi.org/10.1061/(ASCE)0733-9445(1986)112:11(2462)
19. Hordijk DA (1991) Local approach to fatigue of concrete. PhD thesis. Delft, The Netherlands: Delft University of Technology
20. Rots JG (1988) Computational Modeling of Concrete Fracture. PhD thesis. Delft, The Netherlands: Delft University of Technology
21. Jirásek M, Bauer M (2012) Numerical aspects of the crack band approach. Comput Struct 110–111:60–78. https://doi.org/10.1016/j.compstruc.2012.06.006
22. Gupta A, Akbar H (1984) Cracking in reinforced concrete analysis. J Struct Eng 110(8):1735–1746. https://doi.org/10.1061/(ASCE)0733-9445(1984)110:8(1735)
23. Markeset G, Hillerborg A (1995) Softening of concrete in compression - Localization and size effects. Cem Concr Res 25(4):702–708. https://doi.org/10.1016/0008-8846(95)00059-L
24. Angst U, Geiker M, Michel A, Gehlen C, Wong H, Burkan Isgor O et al (2017) The steel-concrete interface. Mater Struct. https://doi.org/10.1617/s11527-017-1010-1
25. Lundgren K (2005) Bond between ribbed bars and concrete. Part 2: The effect of corrosion. Mag Concr Res 57(7):383–395. https://doi.org/10.1680/macr.2005.57.7.383
26. EN 1992-1-1:2005. Eurocode 2: Design of concrete structures - Part 1-1: General rules and rules for buildings. Comité Européen de Normalisation (CEN) Europe. 2005;

27. Mundra S, Rossi E, Malenica L, Pundir M, Angst UM (2025) Precipitation of corrosion products in macroscopic voids at the steel-concrete interface: observations, mechanisms and research needs. Mater Struct. https://doi.org/10.1617/s11527-025-02614-z
28. Ouglova A, Berthaud Y, François M, Foct F (2006) Mechanical properties of an iron oxide formed by corrosion in reinforced concrete structures. Corros Sci 48:3988–4000. https://doi.org/10.1016/j.corsci.2006.03.007
29. Zhao Y, Dai H, Ren H, Jin W (2012) Experimental study of the modulus of steel corrosion in a concrete port. Corros Sci 56:17–26. https://doi.org/10.1016/j.corsci.2011.11.004
30. Xu G, Liu L, Bao H, Wang Q, Zhao J (2017) Mechanical properties of steel corrosion products in reinforced concrete. Mater Struct. https://doi.org/10.1617/s11527-016-0985-3
31. Yates F (1937) The design and analysis of factorial experiments. Imperial Bureau of Soil Science, Harpenden, UK
32. Lundgren K (2002) Modelling the effect of corrosion on bond in reinforced concrete. Mag Concr Res 54:165–173. https://doi.org/10.1680/macr.2002.54.3.165
33. Van Steen C, Van Beirendonck T, Vrijdaghs R, Hendricks MAN, Verstrynge E (2023) A two-phased modelling approach for corrosion-induced concrete cracking and bond deterioration in reinforced concrete. Eng Struct. https://doi.org/10.1016/j.engstruct.2023.116624